Lecture Notes in Electrical Engineering 742

Weiming Ma · Mingzhe Rong ·
Fei Yang · Wenfeng Liu ·
Shuhong Wang · Gengfeng Li *Editors*

The Proceedings of the 9th Frontier Academic Forum of Electrical Engineering

Volume I

Springer

Lecture Notes in Electrical Engineering

Volume 742

The book series *Lecture Notes in Electrical Engineering* (LNEE) publishes the latest developments in Electrical Engineering - quickly, informally and in high quality. While original research reported in proceedings and monographs has traditionally formed the core of LNEE, we also encourage authors to submit books devoted to supporting student education and professional training in the various fields and applications areas of electrical engineering. The series cover classical and emerging topics concerning:

- Communication Engineering, Information Theory and Networks
- Electronics Engineering and Microelectronics
- Signal, Image and Speech Processing
- Wireless and Mobile Communication
- Circuits and Systems
- Energy Systems, Power Electronics and Electrical Machines
- Electro-optical Engineering
- Instrumentation Engineering
- Avionics Engineering
- Control Systems
- Internet-of-Things and Cybersecurity
- Biomedical Devices, MEMS and NEMS

For general information about this book series, comments or suggestions, please contact leontina.dicecco@springer.com.

To submit a proposal or request further information, please contact the Publishing Editor in your country:

China

Jasmine Dou, Editor (jasmine.dou@springer.com)

India, Japan, Rest of Asia

Swati Meherishi, Editorial Director (Swati.Meherishi@springer.com)

Southeast Asia, Australia, New Zealand

Ramesh Nath Premnath, Editor (ramesh.premnath@springernature.com)

USA, Canada:

Michael Luby, Senior Editor (michael.luby@springer.com)

All other Countries:

Leontina Di Cecco, Senior Editor (leontina.dicecco@springer.com)

**** This series is indexed by EI Compendex and Scopus databases. ****

More information about this series at http://www.springer.com/series/7818

Weiming Ma · Mingzhe Rong · Fei Yang ·
Wenfeng Liu · Shuhong Wang · Gengfeng Li
Editors

The Proceedings of the 9th Frontier Academic Forum of Electrical Engineering

Volume I

Springer

Editors
Weiming Ma
Naval University of Engineering
Wuhan, Hubei, China

Mingzhe Rong
Xi'an Jiaotong University
Xi'an, Shaanxi, China

Fei Yang
Xi'an Jiaotong University
Xi'an, Shaanxi, China

Wenfeng Liu
Xi'an Jiaotong University
Xi'an, Shaanxi, China

Shuhong Wang
Xi'an Jiaotong University
Xi'an, Shaanxi, China

Gengfeng Li
Xi'an Jiaotong University
Xi'an, Shaanxi, China

ISSN 1876-1100 ISSN 1876-1119 (electronic)
Lecture Notes in Electrical Engineering
ISBN 978-981-33-6605-3 ISBN 978-981-33-6606-0 (eBook)
https://doi.org/10.1007/978-981-33-6606-0

This Springer imprint is published by the registered company Springer Nature Singapore Pte Ltd.
The registered company address is: 152 Beach Road, #21-01/04 Gateway East, Singapore 189721, Singapore

Committees

Honorary Chairman

Chen Weijiang (Academician of the Chinese Academy of Sciences)

Chairman

Prof. Yang Qingxin (Chairman of China Electrotechnical Society and President of Tianjin University of Technology)
Prof. Rong Mingzhe (Vice President of China Electrotechnical Society and Vice President of Xi'an Jiaotong University)

Academic Committees

Chairman
Ma Weiming (Academician of the Chinese Academy of Engineering)

Vice-Chairman
Cheng Yonghong (Xi'an Jiaotong University)
Prof. Yuan Fuxing (Deputy General Manager of Xi'an High Voltage Apparatus Research Institute)

Secretary-General
Prof. Guo Lijun (Director of Editorial Department of Chinese Journal of Electrotechnical Technology)
Prof. Yang Fei (Xi'an Jiaotong University)

Deputy Secretary-General
Prof. Liu Wenfeng (Xi'an Jiaotong University)
Prof. Liu Dingxin (Xi'an Jiaotong University)

Prof. Wang Laili (Xi'an Jiaotong University)
Prof. Han Xiaogang (Xi'an Jiaotong University)
Prof. Li Gengfeng (Xi'an Jiaotong University)
Prof. Meng Guodong (Xi'an Jiaotong University)
Prof. Michael Tai Ching Fang, University of Liverpool, UK
Prof. Anthony B. Murphy, CSIRO Manufacturing, Australia
Prof. Yasunori Tanaka, Kanazawa University, Japan
Prof. Yann Cressault, Université de Toulouse, France
Prof. Jiudun Yan, University of Liverpool, UK

Organizing Committees

Chairman
Prof. Wang Jianhua (Director, State Key Laboratory of Electrical Insulation and Power Equipment, Xi'an Jiaotong University)

Vice-Chairman
Prof. Li Shengtao (Executive Deputy Dean of Xi'an Jiaotong University)
Prof. Wang Jiansheng (General Manager of Xi'an High Voltage Apparatus Research Institute)

Secretary-General
Wang Wenguang (Deputy Director, Editorial Department, China Electrotechnical Society)
Wang Yusheng (Deputy Director, Editorial Department, China Electrotechnical Society)
Jia Yuquan, Shanghai PIBO Information Technology Center, China
Liang Weihong (Xi'an High Voltage Apparatus Research Institute)
Prof. Wang Shihang (Xi'an Jiaotong University)
Prof. Anthony B. Murphy, CSIRO Manufacturing, Australia
Prof. Yann Cressault, Université de Toulouse, France
Prof. Jiudun Yan, University of Liverpool, UK

Contents

Design of Dynamic Wireless Charging System for Inspection Robot

Xiaokang Wu, Cheng Jiang, Bowei Dong, Hao He, and Songcen Wang

Abstract In this paper, based on the research background of dynamic wireless charging of inspection robot in substation, the magnetic coupling structure and compensation network suitable for wireless charging system of robot are selected, and the transient and steady-state process in the whole process of robot operation is analyzed. According to the analysis results, the corresponding guide rail switching scheme is developed. Combined with the characteristics of the inspection robot that needs precise control, the acceleration sensor and photoelectric sensor collect multiple motion information, accurately locate the robot, and use the FPGA module to process the data in parallel at high speed to control the guide rail at the same time. Finally, the system is verified to be fast by building an experimental platform And the transmission coil on the power supply guide rail is accurately controlled to switch, which ensures the maximum operation power and efficiency of the system.

Keywords Wireless charging · FPGA · Rail switching

1 Introduction

Wireless power transmission technology as a new technology, compared with the traditional electric vehicle wired charging method, has the advantages of no direct contact, convenient charging, small environmental pollution, strong environmental adaptability and so on, so it has been widely valued. However, due to the problems of static wireless charging, such as frequent charging, short range, large battery consumption and high cost, many experts and scholars have conducted extensive research on dynamic wireless charging technology [1–5]. Dynamic wireless charging can be divided into single coil long guide rail type [6, 7] and multi coil segmented

X. Wu · C. Jiang · B. Dong (✉) · H. He · S. Wang
China Electric Power Research Institute, No. 15 Xiaoying East Road, Qinghe, Beijing 100192, China
e-mail: wu6202168@163.com

B. Dong
Beijing Jiaotong University, Haidian District, 3 Shangyuan Village, Beijing 100044, China

W. Ma et al. (eds.), *The Proceedings of the 9th Frontier Academic Forum of Electrical Engineering*, Lecture Notes in Electrical Engineering 742,
https://doi.org/10.1007/978-981-33-6606-0_1

guide rail type [4, 8, 9] according to different layout of transmitting coil. There are many problems of electromagnetic leakage and low transmission efficiency in the layout of single coil long guide rail, while the segmented guide rail reduces unnecessary electromagnetic leakage and energy loss through switching control. Therefore, at present, most of the dynamic wireless charging systems adopt the layout mode of multi transmit coil section guide rail. As one of the important parts of the dynamic wireless charging system, the design of the rail switching system will affect the power and efficiency of the whole system. In this regard, in reference [6], the magnetic field of the transmitting coil is measured in real time through the three-axis magnetic field strength sensor, so as to achieve the purpose of positioning the receiving coil and realize the rail switching control. In Ref. [9], photoelectric sensors are installed on both sides of the transmitting coil to locate the position of the electric vehicle, so as to realize the rail switching. In Ref. [4], the primary coil relay power supply with decentralized control logic is realized by using the secondary active excitation detection. Most of the above literature is about the switching control scheme of electric vehicles. Due to the small receiving coil area, high control accuracy and speed requirements, the robot only operates in a certain area, which is different from the electric vehicle. Therefore, this paper designs a dynamic wireless charging system for wireless charging of inspection robot in substation. Because FPGA chip has the advantages of high-speed parallel processing information [10], the system uses FPGA chip for data processing and system control. The acceleration information of the robot is collected by the acceleration sensor, and the information is transmitted to the control chip through wireless communication. At the same time, the position information of the robot is collected by the photoelectric sensor. After the information is comprehensively processed by the FPGA chip, the control signal is output according to the preset power and efficiency requirements of the wireless charging system, and the control relay is turned on or off, and then the transmitting coil is turned on Switch between on and off.

2 Magnetic Coupling Structure and Compensation Network Design

Magnetic coupling structure is the general designation of transmitting coil and receiving coil in wireless charging system. It can transform high-frequency alternating current into high-frequency magnetic field for energy transmission. Therefore, the selection of magnetic coupling structure has an important impact on the power and efficiency of the system. At present, there are four types of magnetic coupling structure: rectangle circle, rectangle rectangle, circle rectangle and circle circle. For the dynamic wireless charging system designed in this paper, the change of system power and efficiency with the offset distance between the transmitting coil and the receiving coil is the primary index to measure the performance of a dynamic wireless charging system. Therefore, in ANSYS Maxwell, the above four types of magnetic

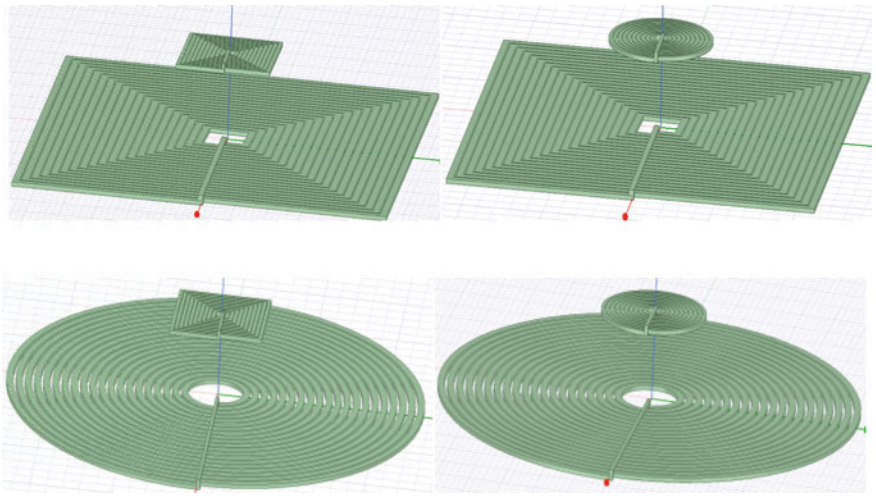

Fig. 1 Magnetic coupling structure simulation diagram

coupling structure are analyzed The magnetic coupling structure is simulated, as shown in Fig. 1.

Under the same control input voltage (200 V), circuit topology (LCC-S), load resistance (5Ω) and other conditions, the power and efficiency of the system change with the offset distance between the transmitting coil and the receiving coil when the system adopts four types of structures: rectangle circle, rectangle rectangle, circle rectangle and circle circle. The results are shown in Fig. 2. Among them, the rectangular transmitting coil is 80 * 80 cm, the rectangular receiving coil is 20 * 20 cm, the circular transmitting coil is 80 cm in diameter, the circular receiving coil is 20 * 20 cm, and the distance between the transmitting coil and the receiving coil is 8 cm.

Through the analysis of the above simulation results, it can be found that the slope of the power and efficiency curve of the system is large when the transmitting coil is of rectangular structure, and will remain at a certain value after reaching the extreme value. When the transmitting coil is of circular structure, the slope of the power and efficiency curve of the system is relatively small, and it keeps growing until the center of the transmitting coil is positive to the center of the receiving coil In addition, the power and efficiency of the receiving coil with rectangular structure is slightly higher than that of the receiving coil with circular structure. For static wireless charging, it is required to have high power and efficiency at a certain fixed position, so it is better to use circular transmitting coil in static wireless charging, but for dynamic wireless charging, it is required that the power and efficiency increase to the maximum value with the offset distance quickly, and can maintain stable power and efficiency at a certain distance, so the transmitting coil is rectangular More suitable for dynamic wireless charging. Considering that the inspection robot is smaller than electric vehicles and trams, which may be affected by external forces in the operation process and lead to the situation of separation from the guide rail, it

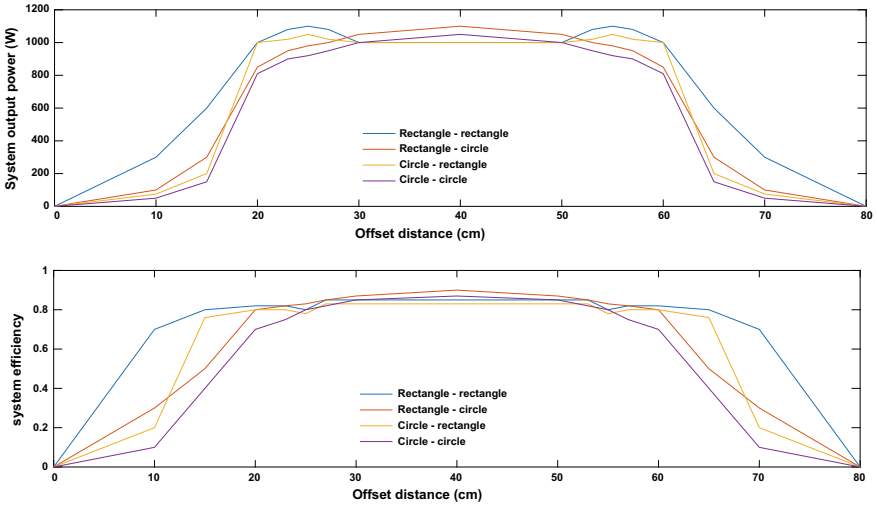

Fig. 2 The variation trend of power and efficiency of the system with the offset distance between transmitting coil and receiving coil

is necessary to select a compensation network that can keep the system current in a safe range when the receiving coil leaves.

The LCC-S circuit structure selected in this paper is shown in Fig. 3. According to Kirchhoff's current law, the AC input current, resonance current on the transmitting coil and resonance current on the receiving coil are calculated as:

$$\begin{cases} I_i = \dfrac{R_p(R_s+R_L)+\omega^2M^2}{X_{Cf}^2(R_s+R_L)}V_i \approx \dfrac{\omega^2M^2}{X_{Cf}^2R_L}V_i \\ I_p = \dfrac{1}{jX_{Cf}}V_i \\ I_s = \dfrac{\omega M}{X_{Cf}(R_s+R_L)}V_i \approx \dfrac{\omega M}{X_{Cf}R_L}V_i \end{cases} \tag{1}$$

After the whole output receiving side leaves, the branch is disconnected, and the current changes to:

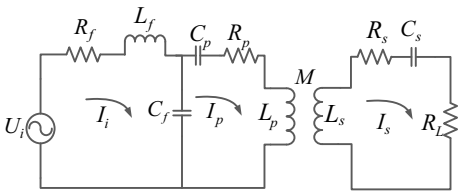

Fig. 3 LCC-S circuit structure

$$\begin{cases} I_i = \dfrac{R_p}{X_{Cf}^2} V_i \\ I_p = \dfrac{1}{jX_{Cf}} V_i \end{cases} \tag{2}$$

It can be found that the system is still in a safe state. Therefore, LCC-S compensation network meets the needs of wireless charging system design of inspection robot.

3 Electromagnetic Transient Analysis of System Switching Process

Wireless charging guide rail switching is divided into soft switching and hard switching. Soft switching refers to reducing the power supply in advance when the inspection robot is about to leave the current guide rail, turning off the guide rail after the power supply voltage drops to 0, opening the next guide rail before the inspection robot enters the next guide rail, and then boosting the power supply to the rated voltage output value. Hard switching refers to patrol inspection When the power supply voltage is not 0, the robot directly turns off the current guide rail or opens the next guide rail. The soft switching mode is to switch at the power supply voltage of 0, so there is no impulse voltage in the system during the switching process, which has high security. However, because it needs time for the power supply to be boosted or depressurized, the power and efficiency of wireless charging in the space passing through during this time will be reduced, so there will be some energy waste in the soft switching mode. In the process of hard switching, the components in the system need to bear impulse voltage, which has certain security risks, and puts forward higher requirements for the withstand voltage of system components. However, when the power and efficiency of the system have not been reduced, the hard switching mode can reduce the energy waste in the soft switching mode.

In order to calculate the maximum impulse voltage of circuit components in hard switching mode, the electromagnetic transient model is established by using the state variable method for the circuit structure in Fig. 1. Define AC input I_i current as state variable x_1, resonant current I_p on the transmitting coil as state variable x_2 Resonance current I_s on receiving coil as state variable x_3, Capacitor voltage C_f is state variable as state variable x_4, Capacitor voltage C_p is state variable as state variable x_5, Capacitor voltage C_s is state variable as state variable x_6. From KCl and KVL:

$$\begin{cases} u_i = R_f x_1 + L_f \dot{x}_1 + x_4 \\ x_5 + R_p x_2 + L_p \dot{x}_2 = M \dot{x}_3 + x_4 \\ L_s \dot{x}_3 + x_6 + R_L x_3 + R_s x_3 = M \dot{x}_3 \\ x_1 = C_f \dot{x}_4 + x_2 \\ x_2 = C_p \dot{x}_5 \\ x_3 = C_s \dot{x}_6 \end{cases} \tag{3}$$

Then the state equation matrix of the system is:

$$\begin{bmatrix} \dot{x}_1 \\ \dot{x}_2 \\ \dot{x}_3 \\ \dot{x}_4 \\ \dot{x}_5 \\ \dot{x}_6 \end{bmatrix} = \begin{bmatrix} -\frac{R_f}{L_f} & 0 & 0 & -\frac{1}{L_f} & 0 & 0 \\ 0 & -\frac{R_p}{L_p} & -\frac{MR_s + MR_L}{L_p(L_s - M)} & \frac{1}{L_p} & -\frac{1}{L_p} & -\frac{M}{L_p(L_s - M)} \\ 0 & 0 & -\frac{R_s + R_L}{L_s - M} & 0 & 0 & -\frac{1}{L_s - M} \\ \frac{1}{C_f} & -\frac{1}{C_f} & 0 & 0 & 0 & 0 \\ 0 & \frac{1}{C_p} & 0 & 0 & 0 & 0 \\ 0 & 0 & \frac{1}{C_s} & 0 & 0 & 0 \end{bmatrix} \begin{bmatrix} x_1 \\ x_2 \\ x_3 \\ x_4 \\ x_5 \\ x_6 \end{bmatrix} + \begin{bmatrix} \frac{u_i}{L_f} \\ 0 \\ 0 \\ 0 \\ 0 \\ 0 \end{bmatrix} \tag{4}$$

From the time domain method, the state transition matrix can be obtained as Eq. (5), where the matrix A represents the coefficient matrix before the state variable in Eq. (4).

$$\phi(t) = e^{At} = 1 + At + \frac{t^2}{2!}A^2 + \cdots + \frac{t^k}{k!}A^k + \cdots \tag{5}$$

The state transition matrix and initial value of system parameters (relay action time is set to 20 ms) are input into Matlab for simulation, the AC input voltage is set to 100 V. The results is:

$$A = 10^7 * \begin{bmatrix} -0.0031 & 0 & 0 & -0.0016 & 0 & 0 \\ 0 & -0.0014 & -0.0014 & 0.0003 & -0.0003 & -0.0001 \\ 0 & 0 & -2.857 * 10^{-14} & 0 & 0 & -0.0024 \\ 1.8169 & -1.8169 & 0 & 0 & 0 & 0 \\ 0 & 9.9010 & 0 & 0 & 0 & 0 \\ 0 & 0 & 4.3346 & 0 & 0 & 0 \end{bmatrix} \tag{6}$$

It can be seen from Eq. (5) that the absolute value of the resonant current on the transmitting coil and the resonant current on the receiving coil is positively related to the variable mutual inductance m, so the maximum value of mutual inductance m shall prevail when calculating the maximum voltage that the element needs to bear. According to the simulation results, when the transmitting coil and the receiving coil center are aligned, the power supply is directly turned off by hard switching mode.

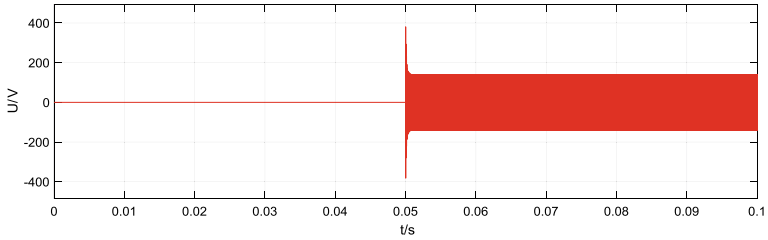

Fig. 4 Voltage and current waveforms of resonant inductors during switching

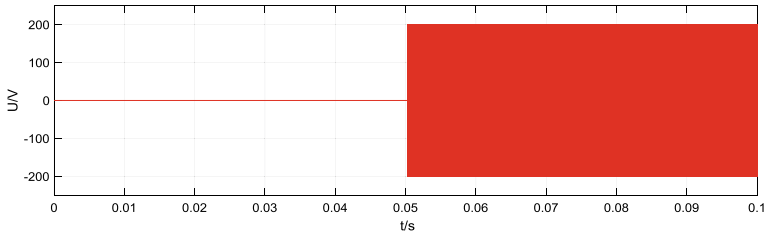

Fig. 5 Voltage and current waveforms of resonant inductors in the improved switching process

In the dynamic components used in the circuit, the series compensation inductor needs to be able to withstand a maximum impulse voltage of about 400 V. In order to further verify the simulation results, the circuit model is built in Simulink and the hard switch off experiment is carried out. The voltage waveform obtained is shown in Fig. 4. It can be seen from Fig. 4 that 400 V impulse voltage will be borne during direct hard switching, which will obviously cause damage to circuit components.

In order to solve this problem, we can choose to add two-stage pre switch in front of the main switch of the original circuit, reduce the voltage of the circuit through two-stage pre switch, and then reduce the impact voltage when the main switch acts. Carry out the hard switch off experiment on the improved circuit model, and the voltage waveform is as shown in Fig. 5. It can be seen from the results in Fig. 5 that the impulse voltage is reduced to about 200 V, which will not cause damage to circuit components.

4 Experiment

In order to verify the above control logic and method, a PCB board with FPGA chip as the core is made as shown in Fig. 6a, and a dynamic wireless charging platform for the simulation robot is built as shown in Fig. 6b. The experimental results show that the whole system can be effectively switched, and the devices in the circuit are not burned. The maximum charging efficiency of the system is 88%, and the maximum output power is 1050 W.

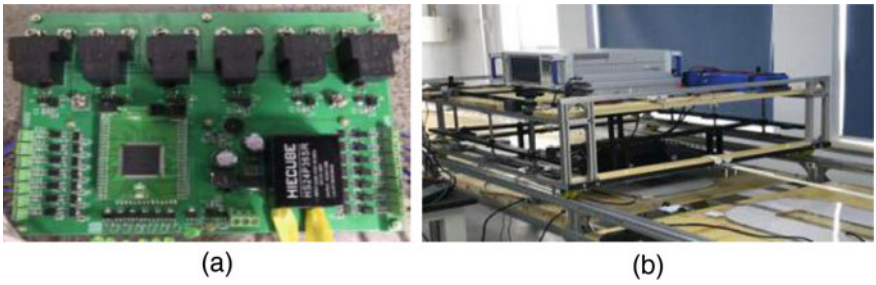

Fig. 6 Experimental site and PCB

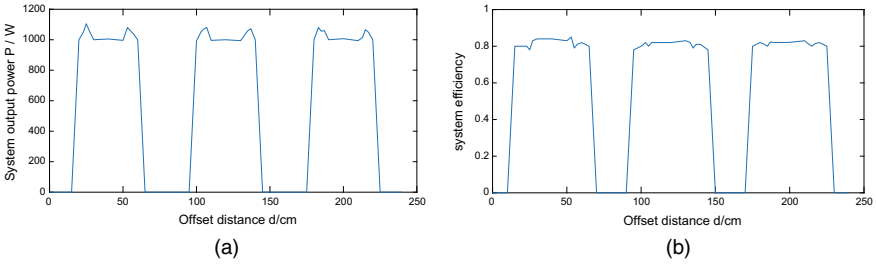

Fig. 7 The transmission power and efficiency of the system

The system output power is shown in Fig. 7a, and the system transmission efficiency is shown in Fig. 7b.

5 Conclusion

This paper mainly studies and designs the dynamic wireless charging of inspection robot from the aspects of magnetic coupling structure, compensation network and switching mode. From the above analysis, it can be seen that for the small dynamic wireless charging system represented by inspection robot, rectangular magnetic coupling structure, LCC-S compensation network and hard switching scheme with front switch can ensure the maximum degree of protection Verify the transmission power and efficiency of the system.

Acknowledgements This work was supported by the Science and Technology Project of State Grid Corporation of China "Research on wireless charging technology of underwater cable inspection robot based on new magnetic device".

References

1. Jili, Lifang Wang, Chenglin Liao, and Shufan Li. 2018. Research and design of radio energy transmission system based on LCL resonance compensation network with automatic side switching charging mode. *Journal of Electrical Technology* 33 (S1): 34–40.
2. Zhang, Xian, Jie Wang, Qingxin Yang, Bin Wei, and Songcen Wang. 2019. Research on electric energy coupling mechanism and switching control of electric vehicle dynamic wireless charging system. *Journal of Electrical Technology* 34 (15): 3093–3101.
3. Wang, Songcen, and Xiu Han. 2019. Study on the design method of bilateral LCC compensation network parameters of magnetic coupling resonance wireless charging system. *Electrical Technology* 20 (06): 12–16.
4. Zhao, Jinbo, Tao Cai, Shanxu Duan, Hao Feng, and Xiaoming Zhang. 2016. Relay method for segmented dynamic wireless charging. *Power System Automation* 40 (16): 64–70.
5. Zhang, Bo., Xujian Shu, and Runhong Huang. 2017. Development of inductive and harmonic radio energy transmission technology. *Journal of Electrical Technology* 32 (18): 3–17.
6. Shin, J., S. Shin, Y. Kim, et al. 2014. Design and implementation of shaped magnetic-resonance-based wireless power transfer system for roadway-powered moving electric vehicles. *IEEE Transactions on Industrial Electronics* 61 (3): 1179–1192.
7. Ko, Y.D., and Y.J. Jang. 2013. The optimal system design of then online electric vehicle utilizing wireless power transmission technology. *IEEE Transactions on Intelligent Transportation System* 14 (3): 1255–1265.
8. Zhu, Wenji, Yue Sun, and Lik Gao. 2016. Multi rail wireless charging method for electric vehicles. *Power System Automation* 40 (18): 97–101.
9. Sun, Yue, Yong Tian, Su. Yugang, and Zhihui Wang. 2013. Efficient distribution scheme of electric vehicle online power supply system. *Journal of Southwest Jiao Tong University* 48 (02): 236–242.
10. Wang, Yi., Ziqiao Deng, Guoliang Ma, Huian Wen, Jun Ye, Xingzhe Hou, Hongliang Sun, and Ke. Zheng. 2018. Design and implementation of multi node power line channel simulator based on FPGA. *Power System Protection and Control* 46 (17): 145–151.

Causes Analysis of Burst Fault for 500 kV Porcelain Bushing Based on Explosion Theory

Jianli Zhao, Yonggang Yue, Zhuo Liu, Shuhua Yao, and Lanjun Yang

Abstract In this paper, a burst fault occurred in the normal operation of a porcelain bushing for 500 kV tank circuit breaker is considered. Based on the explosion theory, the energy range and the mechanism of the chemical and physical explosion of the porcelain bushing were calculated through the analysis of the projective kinetic energy of the porcelain block, the 3D dynamic simulation of the explosion process and the physical and chemical analysis of the ceramic fragments. On this basis, the characteristics and reasons of the explosion of porcelain bushing were systematically analyzed. The results show that the chemical explosion energy of porcelain bushing is estimated as 55–75 g TNT according to the fragmentation distance of porcelain fragments, which is much larger than the energy generated by physical explosion. Thus, the explosion could be considered as chemical explosion. From the physical and chemical analysis of the porcelain fragments and the 3D dynamic simulation results of the explosion process, it could be preliminary conclude that an intensive partial discharge in the porcelain bushing leads to the generation of a large amount of thermal energy. Meanwhile, thermal energy leads to the SF_6 gas filled in bushing rapidly decomposing and expanding which generates gas shock waves and resulting in the explosion. The possible reason of explosion accident could be considered as the abnormal discharge existing in porcelain bushing.

Keywords Porcelain bushing · Explosion theory · Gas shock wave

J. Zhao · Z. Liu · S. Yao
Inner Mongolia Electric Power Research Institute, Hohhot 010020, China

Y. Yue (✉)
Inner Mongolia Extra High Voltage Power Supply Corporation, Huhehaote 010012, Neimenggu, China
e-mail: hvyue@163.com

Y. Yue · L. Yang
College of Electrical Engineering, Xi'an Jiaotong University, Xi'an, Shaanxi 710048, China

W. Ma et al. (eds.), *The Proceedings of the 9th Frontier Academic Forum of Electrical Engineering*, Lecture Notes in Electrical Engineering 742,
https://doi.org/10.1007/978-981-33-6606-0_2

1 Introduction

Tank circuit breaker is a type of circuit breakers, whose arc-extinguishing chamber is in grounded metal box. Meanwhile, as a vital power equipment, tank circuit breaker is widely used in power systems. Bushing is one of the major components of tank circuit breakers, whose main functions include leading high voltage leads inside the equipment to the outside, fixing it, and the components of leads to ground insulation. Furthermore, its safe and stable operation of circuit breaker is related to the safety of the power grid. In 500 kV voltage level system, bushing for tank circuit breaker includes porcelain bushing and composite bushing, whose typical structures are double-shielded structure and single-shielded structure. The double-shielded structure bushing is composed of a pressure equalizing ring, a central conductor, a composite bushing (porcelain bushing), an intermediate shield, a ground shield, and an insulation support. Furthermore, the ground shield is connected to the earth through a metal flange to achieve equipotential to ground. The intermediate shield is made of aluminum material, and it is designed to be suspended in the air. It plays a role of voltage distribution. The main function is to make the electric field between the central conductor and the grounding shield evenly distributed. For the single shield structure, the ground shield exists in while intermediate shielding does not. Although the characteristics of single shielded bushing are simpler structure, easier installation and lower cost, its inner field strength is larger than the double shielded bushing, which is difficult to control. Thus, more accurate design of field strength distribution is required.

On December 17th, 2016, the weather was sunny, and the temperature was below −30 °C. A 500 kV porcelain bushing of tank circuit breaker exploded under the conditions of intact explosion-proof membranes and normal operations. In addition, porcelain fragments were scattered within a range of 60 m, which led damage to a large amount of electrical equipment. Additionally, the safe and stable operation of power grid was affected severely. When the failure occurred, SF_6 low-pressure warning of the fault circuit breaker did not alarmed. Meanwhile, the monitoring system was operating normally. Moreover, from the accident scene, only bushing fragments and some porcelain blocks indicating the presence of ablated glaze could be found. In order to analyze the reasons of the equipment failure, according to the aspects of projectile velocity of the porcelain block, the energy estimation of the porcelain bushing explosion, the porcelain bushing explosion 3D dynamic simulation, porcelain bushing explosion simulation calculation analysis, surface morphology of the porcelain fragmentation, ablation composition analysis, and physicochemical analysis respectively, the research was conducted.

2 Data Measurement and Projectile Velocity Calculation of Exploded Porcelain Fragments

In order to conduct a comprehensive explosion reasons analysis of the porcelain bushing, from the perspective of the energy required for the explosion, the porcelain fragments scattered at accident scene with typical characteristics were collected. 14 points were sampled at accident scene in terms of orientation, distance, and fragments mass respectively. Moreover, the parameters of each porcelain fragment are shown in Table 1. From Table 1, it could be seen that the fragment No. 5 is the heaviest that weighs 48.9 kg. Meanwhile, fragment No. 5 is located north of the center of the explosion, whose projectile distance is 28.2 m. Additionally, fragment No. 14 is second heaviest that weighs 35.3 kg. Simultaneously, fragment No. 14 is located at the southeast direction of the explosion center, whose projectile distance is 18.5 m. As Table 1 indicating, five bushing fragments are larger than 10 kg, which are entirely located at the northeast and southeast directions of the center of the explosion. Therefore, it could be inferred that the explosion position of the bushing might at the east side of the bushing. The basic data should be noticed that SF_6 insulation gas with pressure of 0.6 MPa is filled in the porcelain bushing.

Due to the low flying speed of the fragments, the air resistance could be neglected. Meanwhile, because the porcelain bushing is vertical approximately, the projectile angle of exploded fragments is minor, which means that the ejection angle could be considered as horizontal. The height of the explosion bushing is about 6 m referring to the ground. Through measuring the horizontal distance between porcelain

Table1 Distribution of porcelain fragments at the explosion scene and its related data

Fragments No.	Position (°)	Distance (m)	Mass (kg)	Initial speed (m/s)
1	10	18.0	8.0	16.27
2	20	17.8	27.0	16.09
3	45	18.0	5.5	16.27
4	60	17.9	1.0	16.18
5	90	28.2	48.9	25.48
6	140	29.4	8.5	26.57
7	170	57.9	3.3	52.32
8	195	35.7	7.5	32.26
9	200	32.7	3.0	29.55
10	225	42.0	6.0	37.95
11	250	19.5	9.8	17.62
12	270	28.2	23.6	25.48
13	300	21.3	16.0	19.25
14	315	18.5	35.3	16.72

fragments and explosion point, according to the dynamic equation [1] of the movement of porcelain fragments, it can be obtained that the horizontal initial speed of each porcelain fragment is shown in Table 1. Simultaneously, it could be calculated that the mass weighted average speed is 22.36 m/s. The position is 0° from the east of the center of the explosion. Meanwhile, the measurement direction is rotated counterclockwise.

3 Estimation of Explosion Energy of Porcelain Bushing

3.1 Estimation of Chemical Explosion Energy of Porcelain Bushing

According to the Gurney formula [2] of hollow cylinder charge, the quantity of equivalent explosive (equivalent TNT explosive) required for the porcelain bushing to explode is estimated. The Gurney formula is as following.

$$V_0 = \sqrt{2E}\left(M/C + 0.5\right)^{1/2} \tag{1}$$

where V_0 is the weighted average initial velocity of the porcelain bottle, M is the mass of the porcelain bottle with the quantity of 650–850 kg, C is the mass of the explosive and $\sqrt{2E}$ is a constant which is selected as 2400 m/s. Thus, the energy required for chemical cracking of porcelain bushing could be obtained. Furthermore, the energy required could be equaled to 55–75 g TNT explosive which has a huge power corresponding to the ordinary grenade. Simultaneously, the corresponding chemical explosion energy range is 251–342 kJ (calculation based on 4200 kJ energy could be released from 1 kg TNT).

3.2 Estimation of Physical Explosion Energy of Porcelain Bushing

According to Ref. [1], the physical explosion of a gas cylinder is a decompression expansion process. During the process, the gas in the cylinder is rapidly reduced from high pressure to atmospheric pressure, which is belongs to the explosion of a permanent gas cylinder. Because the explosion time is rapid, it could be considered that the expansion process is performed under the adiabatic state. Therefore, the explosion energy of permanent gas (physical explosion of porcelain bushing) is the work done when the gas expands, which can be expressed by Eq. (2).

$$E_1 = \frac{10pV}{K-1}[1 - (\frac{1}{10p})^{\frac{K-1}{K}}] \times 10^4 \tag{2}$$

where E_1 is the work done f when the gas expands, p is the gas pressure, V is the volume of the porcelain bottle, and K is the specific heat capacity ratio of SF_6 gas. Substituting $p = 0.6MPa$, $V = 0.628m^3$ and $K = 1.095$ into the Eq. (2), the work done by SF_6 gas expansion can be acquired. The physical explosion energy of porcelain bushing equals 57.1 kJ, which is much smaller than the equivalent TNT explosive (between 251 and 342 kJ). Therefore, it can be concluded that the porcelain bushing explosion is not physical explosion filled with high-pressure SF_6 gas, while it should be chemical explosion.

4 3D Dynamic Simulation and Simulation Calculation Analysis of Porcelain Bushing Explosion Process

4.1 3D Numerical Modelling of the Explosion Process of Porcelain Bushing

Applying the AUTODYN finite element software, the fluid–solid coupling method was implemented to model the destruction process of the porcelain shell under the explosive condition of internal explosives. During the modelling process, Euler's algorithm was applied by explosives and air (substitute SF_6 gas). Meanwhile, Lagrange's algorithm was used by porcelain. Through coupling the keywords, axisymmetric models were acquired which are indicated in Figs. 1 and 2.

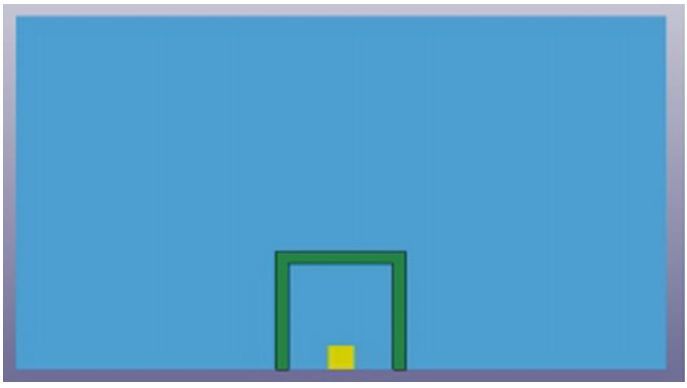

Fig. 1 Finite element explosion model for simulating explosives

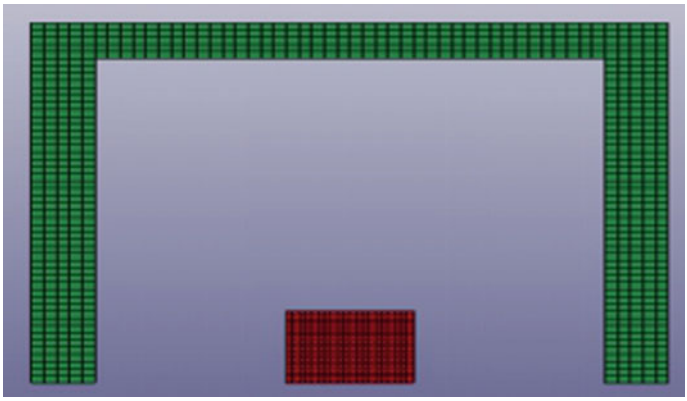

Fig. 2 Grid model for explosives (red) and porcelain bushing (green)

4.2 3D Dynamic Simulation and Simulation Calculation Analysis of Porcelain Bushing Explosion Process

Considering the axisymmetric models in Figs. 1 and 2, excitations were executed to simulate the explosion process of the porcelain bushing. The stress distribution diagram and strain diagram of the porcelain bushing with various explosive time are shown in Fig. 3 and Fig. 4 respectively. The Fig. 3a to f show the stress results at 54 ms, 84 ms, 230 ms, 1300 ms, 1800 ms and 2200 ms respectively. The Fig. 4a to f show the strain distribution at 93 ms, 415 ms, 1017 ms, 1330 ms, 1775 ms and 2200 ms respectively.

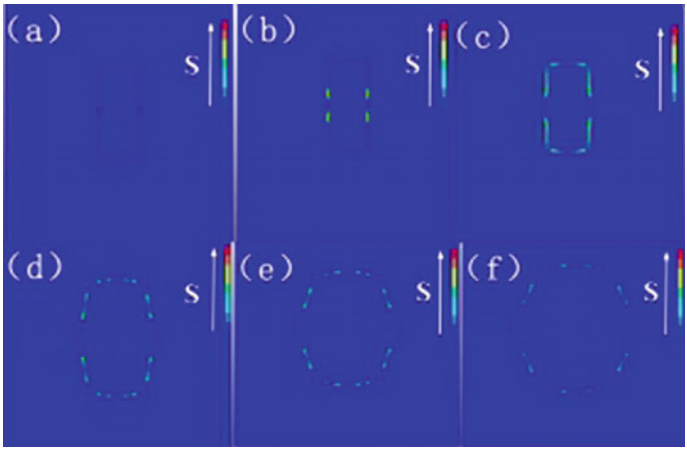

Fig. 3 Stress distribution at different times: **a** 54 μs, **b** 84 μs, **c** 230 μs, **d** 1300 μs, **e** 1800 μs, **f** 2200 μs

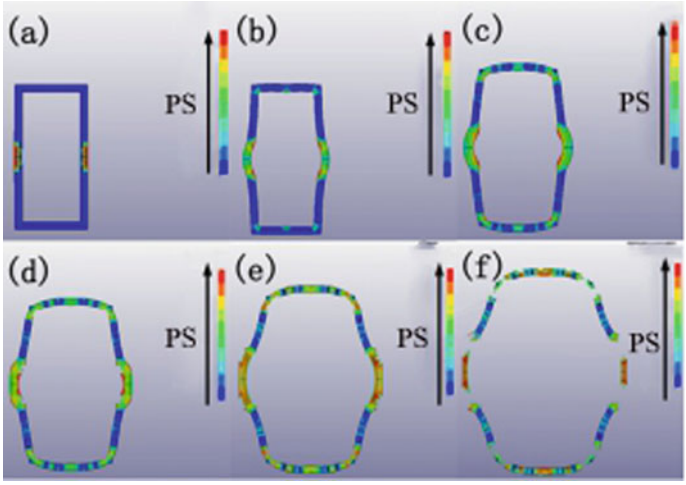

Fig. 4 Plastic strain diagram at different times: **a** 93 μs, **b** 415 μs, **c** 1017 μs, **d** 1330 μs, **e** 1775 μs, **f** 2200 μs

From the comparison of Figs. 3b and 4a, it can be seen that the maximum position of the stress and the maximum position of strain is not coincident. In Fig. 3b, it could be found that the pressure at the shell of the porcelain bushing which is closest to the explosion center is zero. However, as corresponding strain diagram shown in Fig. 4a, the stress is the largest and the stress is distributed on the outer surface of the shell. Because the compression wave propagates to the free surface of the shell, the reflection tensile wave is formed, which lead to the tensile stress forming in the shell. From the comparison of Figs. 3f and 4f, it could be seen that the final fracture of the porcelain bushing occurs at the position of superimposed tensile wave. The above analysis indicates that the explosion of porcelain bushing is caused by the tensile stress generated by the shock wave propagating from the explosion to the outer surface of the porcelain bushing, rather than the ordinary gas pressure increasing and expanding.

5 Physical and Chemical Analysis of Porcelain Fragments

The Hitachi S-4700 Scanning Electron Microscope (SEM) from Japan was used to analyze the surface morphology of the porcelain fragments. The element composition and content on the surface of the fragments were analyzed by the EDAX energy spectrometer of American AMETEK Company. Meanwhile, the set instrument acceleration voltage is 20 kV.